Accepted Manuscript

Title: Fatigue Behavior and Cyclic Deformation of Additive Manufactured NiTi

Authors: Allen Bagheri, M.J. Mahtabi, Nima Shamsaei

PII: S0924-0136(17)30454-5
DOI: https://doi.org/10.1016/j.jmatprotec.2017.10.006
Reference: PROTEC 15426

To appear in: *Journal of Materials Processing Technology*

Received date: 28-12-2016
Revised date: 30-9-2017
Accepted date: 1-10-2017

Please cite this article as: Bagheri, Allen, Mahtabi, M.J., Shamsaei, Nima, Fatigue Behavior and Cyclic Deformation of Additive Manufactured NiTi.Journal of Materials Processing Technology https://doi.org/10.1016/j.jmatprotec.2017.10.006

Fatigue Behavior and Cyclic Deformation of Additive Manufactured NiTi

Allen Bagheri[1], **M.J. Mahtabi**[1], and **Nima Shamsaei**[2,*] (*Corresponding Author*)

[1]Department of Mechanical Engineering and Center for Advanced Vehicular Systems (CAVS), Mississippi State University, MS 39762, USA
[2]Laboratory for Fatigue & Additive Manufacturing Excellence (FAME), Department of Mechanical Engineering, Auburn University, Auburn, AL 36849, USA

*Phone: (+1) 334-844-4839, E-mail: shamsaei@auburn.edu

Submitted to:
Journal of Materials Processing Technology

Original Submission: December 2016
Revised Submission: September 2017

Abstract

The aim of this study is to experimentally investigate the fatigue behavior of additively manufactured (AM) NiTi (i.e. Nitinol) specimens and compare the results to the wrought material. Additive manufacturing is a technique in which components are fabricated in a layer-by-layer additive process using a sliced CAD model based on the desired geometry. NiTi rods were fabricated in this study using Laser Engineered Net Shaping (LENS), a Direct Laser Deposition (DLD) AM technique. Due to the high plateau stress of the as-fabricated NiTi, all the AM specimens were heat-treated to reduce their plateau stress, close to the one for the wrought material. Two different heat treatment processes, resulting in different stress plateaus, were employed to be able to compare the results in stress- and strain-based fatigue analysis. Strain-controlled constant amplitude pulsating fatigue experiments were conducted on heat-treated AM NiTi specimens at room temperature (~24°C) to investigate their cyclic deformation and fatigue behavior. Fatigue lives of AM NiTi specimens were observed to be shorter than wrought material specifically in the high cycle fatigue regime. Fractography of the fracture surface of fatigue specimens using Scanning Electron Microscopy (SEM) revealed the presence of microstructural defects such as voids, resulting from entrapped gas or lack of fusion and serving as crack initiation sites, to be the main reason for the shorter fatigue lives of AM NiTi specimens. However, the maximum stress level found to be the most influential factor in the fatigue behavior of superelastic NiTi.

Keywords: Fatigue; Cyclic Deformation; Additive Manufacturing; Shape Memory Alloys; Failure Mechanisms; Fractography

Nomenclature

AM	Additive Manufacturing / Additively Manufactured
A→M	Austenite to martensite transformation
DLD	Direct Laser Deposition
E_A	Austenite modulus
E_M	Stress-induced martensite modulus
HCF	High Cycle Fatigue
HT	Heat Treatment/Heat-treated
LCF	Low Cycle Fatigue
LENS	Laser Engineered Net Shaping
MCF	Mid Cycle Fatigue
$2N_f$	Number of reversals to failure
N_f	Number of cycles to failure
ε_{max}	Maximum strain
ε_{min}	Minimum strain
ε_s^{AM}	A→M start strain
ε_f^{AM}	A→M finish strain
σ_s^{AM}	A→M start stress

1. Introduction

NiTi (i.e. Nitinol) is an almost equiatomic alloy of nickel and titanium and exhibits unique properties such as shape memory and superelasticity (also called pseudoelasticity). Shape memory is the ability of the material to recover a plastic strain by heating the material to above a certain temperature, while superelasticity is the capability of the material to recover strain levels as large as 4%-8% by just unloading. Because of these properties as well as its considerable resistance to severe environmental conditions, NiTi has been utilized in various applications in automotive, aerospace and biomedical industries. Hartl and Lagoudas (Hartl and Lagoudas, 2007) discussed some applications of NiTi in aerospace industry, including the Boeing variable geometry chevron. Carpenter and Lyons (Carpenter and Lyons, 2001) listed other applications for NiTi, such as structural connectors, seals, vibration dampers, release or deployment mechanisms. Some applications of NiTi in seismic isolation and energy dissipation were also mentioned by Azimi et al. (Azimi et al., 2017). Plotino et al. (Plotino et al., 2009) listed endovascular stents, endodontic files, and vena cava filters as some examples of NiTi application in the biomedical industry. In addition, Moghaddam et al. (Moghaddam et al., 2014) utilized NiTi for bio-implants where an appropriate combination of mechanical properties as well as biocompatibility is needed. In such applications, however, the main challenge is the size and geometry of the implant, which is patient-injury dependent, making the design and fabrication of the implant somewhat complicated.

The process of fabricating NiTi parts with complex geometries using conventional techniques, such as machining, metal stamping, forging, casting and powder metallurgy, is excessively difficult. Wu (Wu, 2002) reported that machining of NiTi parts, although possible, is cumbersome due to the work hardening property of the material. Moreover, Drexel et al. (Drexel et al., 2007) showed that the mechanical properties of NiTi, such as modulus of elasticity and loading/unloading stress plateaus, are very sensitive to the manufacturing and post-manufacturing

processes such as the amount of prior cold work as well as heat treatment time and temperature. For instance, the loading and unloading stress plateau levels are highly sensitive to the temperature difference between the operating temperature and the austenite finish temperature, A_f. Pelton et al. (Pelton et al., 2000) found that the transformation temperatures of NiTi alloys vary significantly by altering the heat treatment process. Rahim et al. (Rahim et al., 2013) observed that the existence of an insignificant amount of impurities such as oxygen content would also cause a large variation in the mechanical properties of this alloy including its fatigue strength.

Otsuka and Wayman (Otsuka and Wayman, 1999) reported vacuum arc melting (VAM) and vacuum induction melting (VIM) followed by casting, hot working or cold working with intermediate annealing and finally shape memory treatment, as the most commonly used commercial methods to produce NiTi components. Due to the high affinity of titanium towards oxygen, the melting process in these methods has to be conducted in a vacuum or inert atmosphere. Due to the small molten zone, produced as the arc progressively melts the electrode in the VAM process, there will be a less homogeneous distribution in chemical composition along the ingot. As a result of the variation in the chemical composition from top to bottom of the ingot, the transformation temperatures may vary more than 10˚C along the height.

Wu (Wu, 2002) found that by repeating the vacuum arc re-melting process, so called multiple melting process, a more homogeneous ingot may be achieved. In addition, Wu demonstrated that the vacuum induction melting process has the drawback of crucible contamination to calcia (CaO) or graphite, meaning that molten NiTi may pick up carbon contaminants from the crucible, which in turn may change the transformation temperature. Finally, Hey and Jardine (Hey and Jardine, 1994) demonstrated that the main problem related to the casting process of NiTi is the presence of

high level of microstructural defects, which can significantly affect the mechanical behavior and fatigue performance of the product.

Various fabrication processes have been developed in order to overcome the issues related to the melting process and conventional machining of NiTi parts. Accordingly, Bram et al. (Bram et al., 2002) utilized powder metallurgy methods like hot isostatic pressing (HIP), Chu et al. (Chu et al., 2004) employed self-propagating high-temperature synthesis (SHS), Schüller et al. (Schüller et al., 2004) used metal injection molding, and normal sintering to fabricate NiTi components. In powder metallurgy techniques, since the pressure has to be applied equally from all directions, fabrication of parts with more complex geometries becomes increasingly challenging.

Laser Engineered Net Shaping (LENS) is a Direct Laser Deposition (DLD) additive manufacturing (AM) technique where the metal powder is injected into the melt pool created from a laser beam. This process is repeated and consecutive layers are built along the height in order to fabricate the desired geometry. This method, first developed by Sandia National Laboratories in the late 1990s (Griffith et al., 1996), provides the ability of producing and cladding metallic materials (i.e. Inconel 625, H13 tool steel and 316 stainless steel, etc.) with complex geometries, which are difficult to fabricate by the conventional manufacturing techniques. Gu et al. (Gu et al., 2012) showed that the DLD process is a unique technique for rapid prototyping/manufacturing and product repair due to its cost-saving potential, as well as its ability to produce fine microstructures and create functionally-graded compositions. However, Shamsaei et al. (Shamsaei et al., 2015) demonstrated that utilizing AM processes to fabricate structural components still has major challenges due to the AM materials (i.e. Ti-6Al-4V, 316 stainless steel, 316L stainless steel, Inconel 738, etc.) possessing different microstructure, mechanical and, more importantly, fatigue properties as compared to their wrought counterparts. Frazier (Frazier, 2014) showed that the

complex thermal profile applied to the AM parts/alloys (i.e. Ti-6Al-4V, Al-Si-Mg, H13 Steel, IN625, 316 stainless steel, 316L stainless steel, etc.) during the fabrication process, complicates analyzing the microstructural evolution and resulting features. These thermal profile features include directional heat extraction, repeated melting, and rapid solidification, which are not involved in conventional fabrication methods. Frazier (Frazier, 2014) also stated that in many of the AM processes, relatively high cooling rates are experienced by the material, which results in reduced partitioning and smaller grain sizes. Although processing defects, such as micro-pores,) are known to dominate the fatigue properties of AM produced alloys. Shao et al. (Shao et al., 2017) showed that post-fabrication techniques, such as hot isostatic pressing (HIP), can reduce these process-induced defects.

Bagheri et al. (Bagheri et al., 2015) achieved different microstructure and mechanical properties for Ti-6Al-4V by adjusting various process parameters such as laser power, beam travel speed, layer thickness, and powder feed rate, resulting in different thermal histories. Shamsaei et al. (Shamsaei et al., 2015) discussed that different thermal histories, subsequently, may create a non-homogeneous, anisotropic microstructure with inevitable porosity and defects in AM materials. Bian et al. (Bian et al., 2015) showed that monotonic mechanical properties of AM metallic material (Ti-6Al-4V), such as tensile and compressive strengths, as well as hardness, are generally comparable to, or even higher than, wrought and cast materials, due to a higher cooling rate during the AM process, resulting in finer microstructures. For instance, Shishkovsky and co-workers (Shishkovsky et al., 2012) studied the microhardness of AM NiTi specimens and reported the AM specimens to be 1.5-2 times harder than those fabricated by casting. They explained this increase in the microhardness by the additional hardening of the NiTi matrix caused by the rapid cooling during the AM process. Elahinia et al. (Elahinia et al., 2016) reported that the rapid cooling process

imposed in AM techniques introduces an increased level of residual stress in the resulting parts (NiTi parts) and forms martensitic grains. Saedi et al. (Saedi et al., 2016b) investigated the effect of post-fabrication heat treatments, such as solution annealing (950 °C, 5.5 h, H2O) and subsequent aging (350 °C and 18 h, and 450 °C for 10 h) on hardness of Ni-rich NiTi samples fabricated using selective laser melting (SLM) technique. They showed that SLM-fabricated NiTi shows significantly lower hardness compared to the original ingot. However, solution annealing could recover the hardness of the AM NiTi and increase it to a hardness even higher than the original ingot. The effect of solution annealing on increasing the hardness was explained by the fact that solution annealing solves the brittle Ni_4Ti_3 precipitates, which reduces the brittleness. The subsequent aging was also reported to gradually increases the hardness.

Meier et al. (Meier et al., 2011) studied the monotonic compressive behavior of SLM-fabricated Ti-rich ($Ni_{50.2}Ti$) specimens in different orientations with respect to the building direction and compared the results to the ones for wrought NiTi. They concluded that the compressive behavior of the AM NiTi samples was not affected by the fabrication orientation. Their results can be justified by the fact that during compression, localized defects (e.g., small pores and particles) in the sensitive regions (i.e. the interface between the layers) are collapsed and may not contribute as much to the failure of the specimen. The Ti-rich SLM NiTi specimens in (Meier et al., 2011) exhibited similar monotonic compressive behavior to the one from conventional NiTi.

Bernard et al. (Bernard et al., 2012) studied the cyclic compression fatigue behavior of porous additive manufactured NiTi parts produced by LENS® technology. They reported runout for all of the specimens tested at stress levels up to the compressive transformation stress of the material. They reported an increase in the permanent deformation of the NiTi specimens, by increasing number of cycles and/or stress level. However, at a certain stress level, the permanent deformation

appeared to saturate after a limited number of cycles of loading. Bernard et al. (Bernard et al., 2012) also reported an inverse relation between the amount of porosity and the final permanent deformation. In other words, they observed that as the porosity increased, the permanent deformation decreased.

Speirs et al. (Speirs et al., 2017) studied the fatigue behavior of different NiTi unit cell designs manufactured via SLM technique. They reported the fatigue resistance of the SLM-fabricated NiTi components to highly depend on the geometry of the part, which could be attributed to the surface topography and notch sensitivity. Moreover, they reported high compressive fatigue resistance for the SLM-fabricated NiTi parts, demonstrating the appropriateness of these components for implant application. Mahtabi et al. (Mahtabi et al., 2015a) demonstrated that although fabricating NiTi components using AM techniques has recently become very popular, fatigue performance of these components is still the main challenge against the adoption of these techniques in load bearing applications.

Although extensive investigations have been conducted in the past two decades to study the fatigue behavior of NiTi materials fabricated by traditional techniques, fatigue data for AM NiTi are not readily available in the literature and the effects of manufacturing induced defects on their fatigue resistance are unknown. Mahtabi and Shamsaei (Mahtabi and Shamsaei, 2016) concluded that this is partially due to the AM techniques being relatively new and in part because of difficulties due to the fretting fatigue involved in fatigue testing of NiTi specimens, especially in high cycle regime. Therefore, the aim of this study is to investigate the uniaxial fatigue behavior and failure mechanisms of superelastic NiTi specimens, manufactured using LENS, under strain-controlled pulsating ($R_\varepsilon = 0$) cyclic loads. Various aspects of the fatigue behavior of AM NiTi are compared to the wrought counterpart and results are discussed.

2. Material and Experimental Program

Spherical gas atomized NiTi powder (-100/+325 mesh), produced based on ASTM standard (ASTM B214−15, 2011), was utilized to fabricated the AM NiTi rods in this study. Ni-rich NiTi was used in this study due to its extensive application in biomedical engineering. The chemical composition of the powder included 55% nickel and 43% titanium in weight percent (50.7% Ni-48.6%Ti in atomic percent). Details of the chemical composition of the powder are listed in Table 1.

Table 1. Chemical composition of NiTi powder used to fabricate specimens in this study.

Element	O	Al	C	Fe	H	N	Cr	Ni	Ti
Weight percent (%)	0.10	0.009	0.017	0.009	0.002	0.008	0.19	55.0	43.0

The scanning electron microscopy (SEM) image of the powder, given in Fig. 1a, shows that all the particles were spherical. Fig. 1b plots the particle size distribution and indicates the range of the majority of the particle size to be from 30 μm to 150 μm.

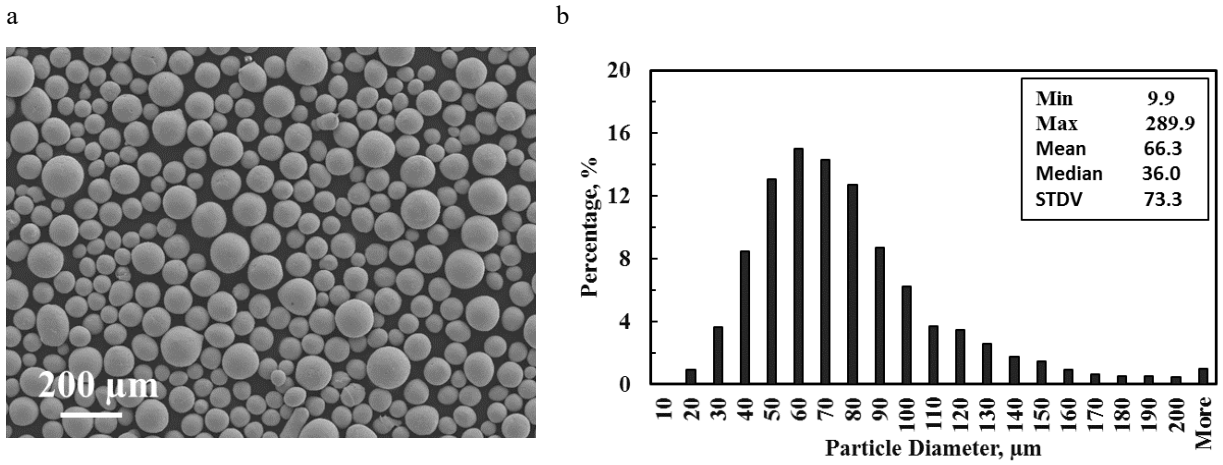

Fig. 1. (a) Scanning Electron Microscopy (SEM) micrograph of NiTi powder, and (b) size distribution of the powder.

An OPTOMEC LENS® 750 machine, retrofitted with 1 kW laser source (Nd:YAG) was utilized to fabricate the AM specimens. NiTi rods of 8 mm diameter and 80 mm height, as shown in Fig. 2a, were manufactured at room temperature one at a time (single-built), vertically on a pure

titanium (grade 5) substrate. The oxygen level was kept less than 5 ppm during manufacture, resulting in negligible amount of oxide in the NiTi specimens as revealed by post-fabrication analysis using EDX.

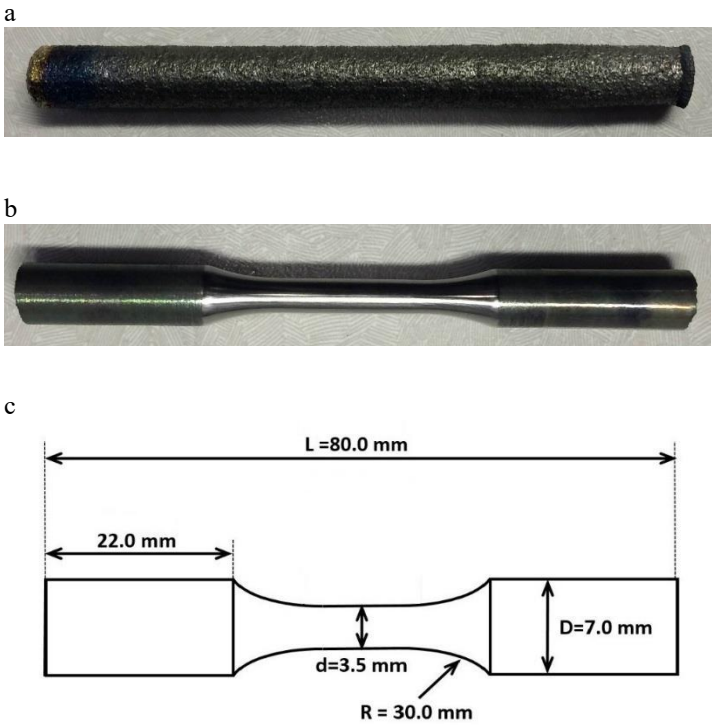

Fig. 2. (a) As-Fabricated NiTi rod, (b) machined specimen, and (c) drawing of the fatigue specimen.

The LENS process parameters, i.e. laser power, scanning speed, powder feed rate, and layer thickness, utilized in manufacturing of NiTi bars are listed in Table 2. These parameters were selected through a process optimization study, based on the objective to obtain a high level of density for the AM material with reference to the wrought NiTi. The density of the AM bars was calculated based on the Archimedes' principle and the process parameters were selected to achieve an average density of 99.8% of that the one for wrought NiTi.

Table 2. Process parameters used for fabricating NiTi specimens by LENS.

Laser power (W)	Scanning speed (mm/s)	Powder feed rate (g/s)	Layer thickness (mm)
280	8.47	0.06	0.2

As-fabricated NiTi bars were centered to ensure a constant diameter over the length of the bar and provide a smooth surface in the grip section. The centered bars then were machined to standard cylindrical specimens with uniform gage section with a 3.5 mm diameter, according to ASTM standard for strain-controlled fatigue testing (ASTM E606 / E606M-12, 2012). A picture of the machined specimen is presented in Fig. 2b and the drawing of the specimens, illustrating the dimensions of the different sections, is shown in Fig. 2c.

Machined cylindrical specimens were heat-treated in two different conditions. For the first heat treatment (HT1), the samples were aged at 550 °C for 60 min and cooled in air. Heat treatment 2 (HT2), however, included two steps: aging at 550 °C for 180 min and cooling in air, followed by solution annealing at 550 °C for 3 min and water quenching. Both heat treatments were selected to obtain a superelastic material at room temperature. It is also worth mentioning that the corresponding heat treatments for AM specimens were selected by trial and error so that two sets of specimens (i.e. AM HT1 and AM HT2) exhibit two different stress plateau levels, which enables investigating the fatigue behavior in strain-life and stress-life approaches. Gage sections of all the fatigue specimens were mechanically polished to minimize the effects of surface flaws on the fatigue life. In this case, sand papers from a rough level (girt #320) to a smooth level (girt #4000) were used to polish all the specimens. Both monotonic and cyclic tests were performed in air and at room temperature (~ 24 °C). Microstructure of the heat-treated wrought and two AM NiTi specimens are shown in Fig. 3. In this figure, each column is related to different locations on the specimen (e.g. left, center and right location of the cross-section).

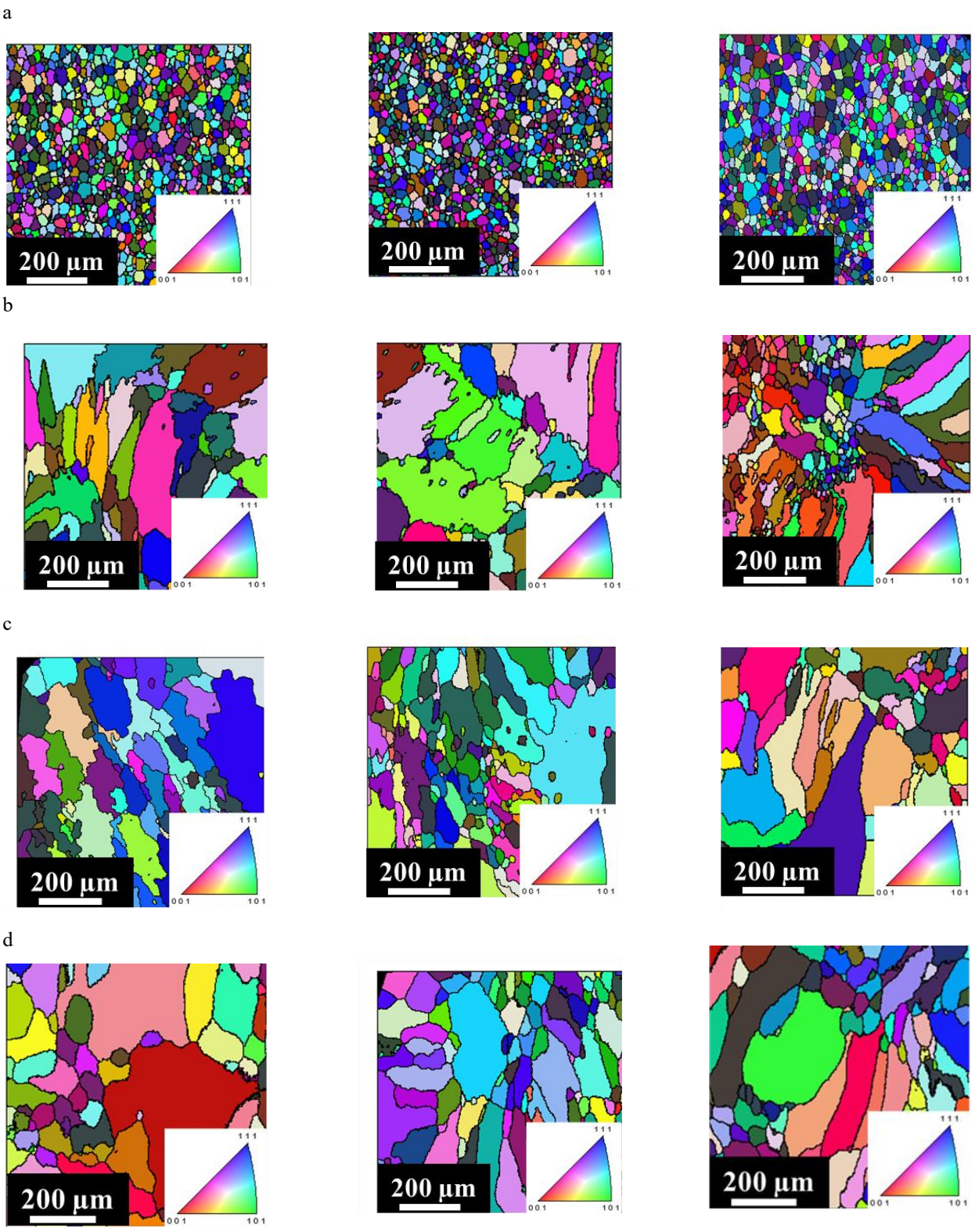

Fig. 3. EBSD colored map of microstructure of (a) wrought, (b) AM as-built specimens (c) AM HT1, and (d) AM HT2, indicating the grain shape, size, and orientation.

As can be seen in Fig. 3a, grains in the heat-treated wrought NiTi are uniformly distributed over the section of the specimen with an average grain size of ~5 μm and an aspect ratio of approximately one. AM specimens, however, show entirely different microstructure with significantly larger grain size and aspect ratio, as can be noticed from Figs. 3b, c and d. As-built AM specimens, shown in Fig. 3b, appear to have an average grain size of about 13 μm. AM HT1 specimens, shown in Fig. 3c, seem to have larger grain size due to lower cooling rate after annealing (cooled in air). The average grain size for this specimen was about 23 μm. AM HT2 specimens, which were quenched in iced water and underwent a very high cooling rate, has considerably smaller average grain size, as depicted in Fig. 3d, compared to AM HT1 specimen. The average grain size for this specimen was about 17 μm. It should be noted that both AM HT1 and HT2 specimens have experienced a similar fabrication process and are expected to inherit similar microstructures before the heat treatment process. Therefore, the observed different microstructure of these two specimens can be attributed to the effects of different heat treatments. Several different types of precipitate particles (e.g., Ni_4Ti_3, Ni_3Ti particles) can form during heat treatment of NiTi (Otsuka and Ren, 2005). Presence of these precipitates can influence the martensitic phase transformation in NiTi and, subsequently, affect the stress-strain response of the alloy (Gall et al., 1998).

Saeidi et al. (Saeidi et al., 2016a) demonstrated that post-fabrication aging with precipitation hardening can improve the strength of the SLM-fabricated $Ni_{50.8}Ti_{49.2}$ alloy. Moreover, solution annealing of AM NiTi can form new precipitate particles in the material, which may improve the superelastic behavior of the alloy. Nishida et al. (Nishida et al., 1986) suggested heat treatment as one of the most effective means of controlling the transformation temperatures and increasing the strength of Ni-rich NiTi alloys. They explained the changes in the material behavior to the

formation of Ni_4Ti_3, Ni_3Ti_2, and Ni_3Ti precipitates. Karaca et al. (Karaca et al., 2013) indicated that the precipitates characteristics, such as size, volume fraction and inter-particle space, determine strengthening ability of precipitation in NiTi. They stated that fine and coherent precipitates have strengthening effects on the matrix and can increase the thermal stability; however, there might be a reduction in the transformation temperatures. Furthermore, shape memory properties of NiTi alloys including matrix composition, transformation strain, and critical transformation stress could be altered by precipitates. Sehitoglu et al. (Sehitoglu et al., 2001) studied the cyclic deformation of single crystal NiTi and reported the response of this alloy to be highly associated with the orientation and texture of the grains.

An MTS 810 uniaxial servo-hydraulic test system was used to perform all the monotonic tests on AM specimens, in a strain-controlled condition up to fracture. All the fatigue tests were conducted in pulsating strain-controlled condition (i.e. $R_\varepsilon = \varepsilon_{min}/\varepsilon_{max} = 0$) at different maximum strain levels of ε_{max}= 0.6%, 0.7%, 0.8%, 0.9%, 1.0%, 1.4% and 2.0% using an MTS 858 uniaxial servo-hydraulic testing machine. An MTS uniaxial extensometer with a gage length of 15 mm was used to measure and control the strain. All the cyclic tests were conducted at a constant average strain rate, comparable to that used for testing wrought material (Mahtabi et al., 2015b). A Laser thermometer was used to monitor the temperature at the gage section of selected specimens, and the results indicated that the temperature change was not significant (less than 1 °C) during the cyclic test. Scanning Electron Microscopy (SEM) was used to observe the fracture surface of the fatigue specimens and study the crack initiation and propagation characteristics.

3. Deformation Behavior and Discussion

3.1 Monotonic Tensile Behavior

As shown in Fig.4 for wrought NiTi, stress–strain response of superelastic NiTi is generally comprised of four different regions: the first linear region, formed by initial loading, can be

described as elastic loading of the austenite phase. The second region of the stress-strain curve (the almost flat region) is associated with the stress-induced martensitic transformation (yield-like behavior). After the material is fully martensitic (i.e., end of the second region), the material behaves like other metallic materials and exhibits a second linear-elastic region (with a different modulus of elasticity) on the stress-strain curve. Beyond this region, there will be another yielding region, where plastic deformation will dominate the deformation of the material, as described by Tan et al., (Tan et al., 2004).

Tensile stress-strain curves of AM NiTi specimens, from monotonic tests, are compared with the one for wrought material in Fig. 4. The data related to the wrought material are from the coauthors' recent work (Mahtabi et al., 2015b). As can be seen in this figure, the two heat treatment processes, selected for the AM NiTi specimens, resulted in plateau stresses somewhat comparable to the plateau stress of the wrought material. Fig. 4 also illustrates that the elongation to failure was ~ 4% and ~ 5% for AM HT1 and HT2 specimens, respectively, as compared to ~ 12% for the wrought counterpart. This indicates that, similar to other materials fabricated by LENS (Yadollahi et al., 2015), AM NiTi specimens exhibit shorter elongation to failure than the wrought NiTi.

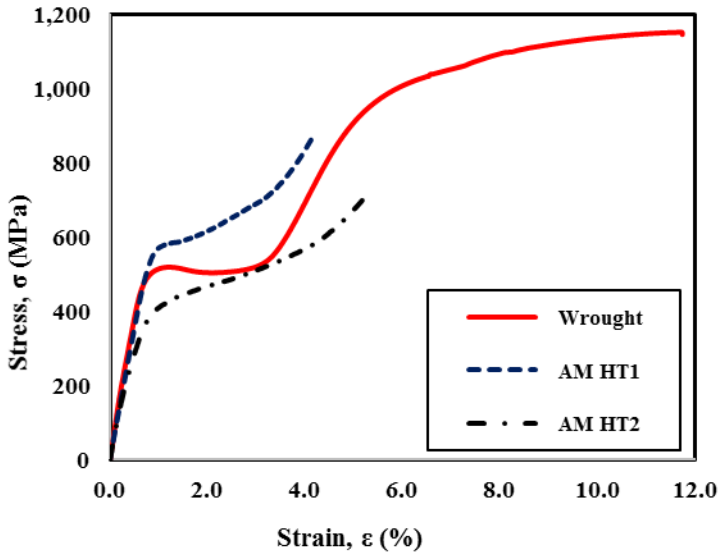

Fig. 4. Comparison of the monotonic tensile stress-strain response of the wrought (Mahtabi et al., 2015b) and AM NiTi.

Tensile specimens in all three conditions had a flat fracture surface with no indication of necking before final fracture. However, as shown in Fig. 5, dimples were observed on the fracture surface of both wrought and AM specimens, depicting a ductile fracture under tensile loading. Larger and deeper dimples, observed on the fracture surface of the wrought specimen (right column of Fig. 5a), can explain the larger elongation to failure and ductility, observed for this sample as compared to AM specimens. Presence of the microstructural defects such as voids (middle column of Figs. 5b and c), resulting from entrapped gas and/or un-melted regions, due to lack of fusion and/or low laser penetration depth, may have contributed to the smaller elongation to failure of AM specimens.

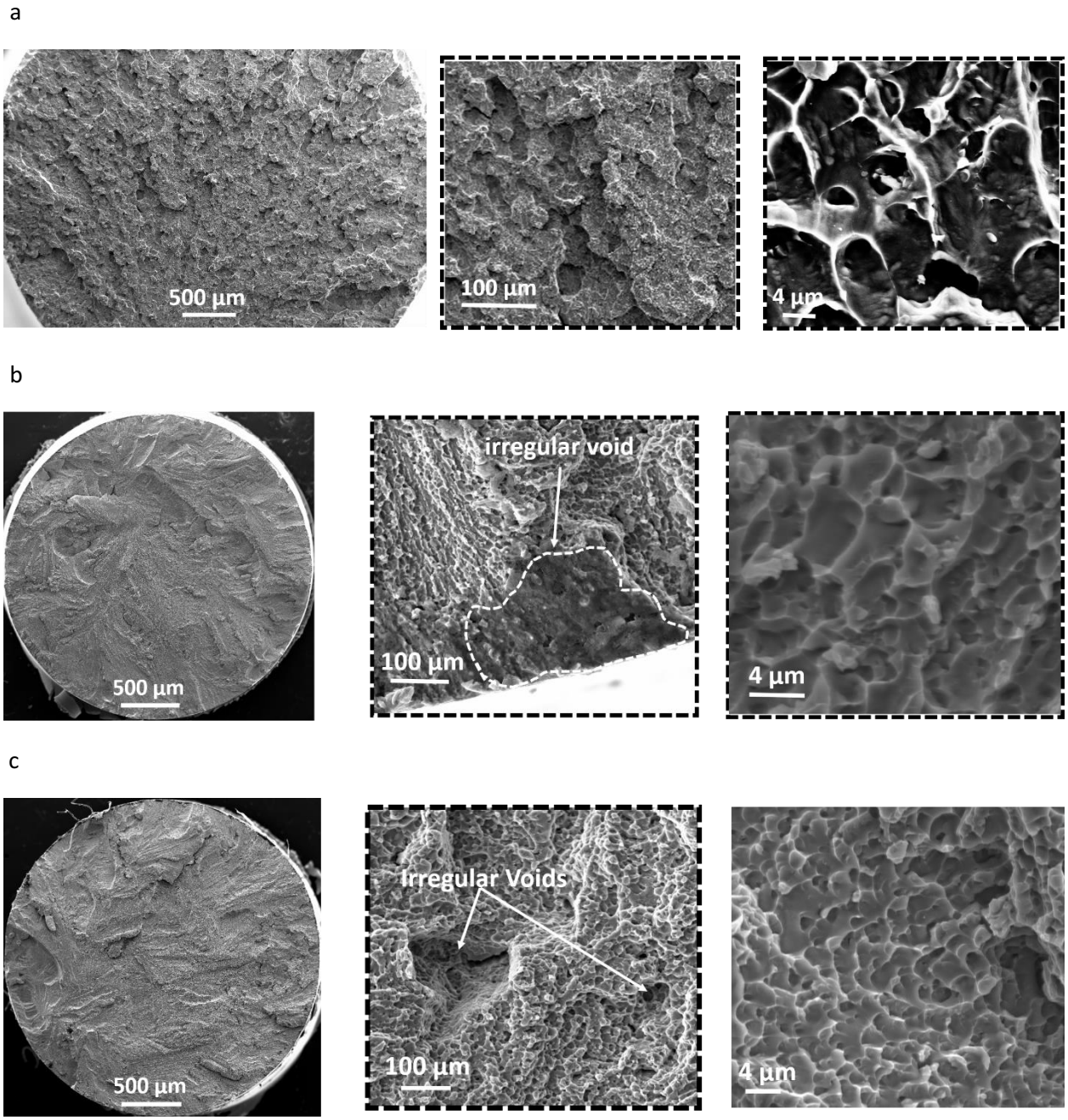

Fig. 5. Fracture surfaces of tensile specimens for: (a) wrought, (b) AM HT1, and (c) AM HT2 exhibiting dimples as evidence of ductile fracture.

Tensile material properties, such as loading stress plateau and modulus of elasticity measured for wrought and AM specimens under monotonic loading are presented in Table 3. The results from monotonic tensile experiments demonstrate the austenite modulus, E_A, of wrought material and AM HT1 specimen to be 73 GPa, while that for AM HT2 specimen was found to be lower and

around 58 GPa. Obtaining a low austenite modulus of elasticity for the AM HT2 specimen, compared to HT1, indicates that the modulus of elasticity, as well as other mechanical properties of NiTi such as stress plateau can be adjusted to desired, application-specific values. This capability becomes promising, especially for the biomedical industry, knowing that the mechanical properties of AM NiTi may be adjusted to that of the human bone, providing a more durable, compatible, and effective implant. The modulus of the stress-induced martensite region, E_M, for the wrought NiTi was reported to be ~ 22 GPa (Mahtabi et al., 2015b), while E_M could not be measured for the AM material since the specimens fractured before reaching the fully martensitic region of the stress-strain curve. Furthermore, the stress-induced phase transformation appears to start at ~1.0% for all three sets of specimens.

Table 3. Tensile properties of wrought (Mahtabi et al., 2015b) and AM NiTi specimens used in this study.

Property	Wrought	AM HT1	AM HT2
Austenite modulus, E_A	~73 GPa	~73 GPa	~58 GPa
A→M start stress, σ_s^{AM}	~515 MPa	~580 MPa	~430 MPa
A→M start strain, ε_s^{AM}	1.0%	1.0%	1.0%

3.2 Cyclic Deformation Behavior

Stress-strain response of the first cycle of loading at different strain levels for both wrought and AM NiTi specimens are presented in Fig. 6. As shown for the wrought material, the stress-induced martensite start strain, ε_S^{AM}, is about 1.0% and the specimen exhibits a nearly perfect superelastic behavior, as it recovers all the applied strain with almost zero residual strain. Similarly, the first cycle responses of both AM NiTi specimens, heat-treated under two different thermal processes (i.e. HT1 and HT2), illustrate a fully superelastic response, as presented in Figs. 6b and c. This

behavior is at least valid for strain levels up to 2.0%. Analogous to the wrought specimen, the A→M start strain for both types of AM specimens appear to be around 1.0%.

a

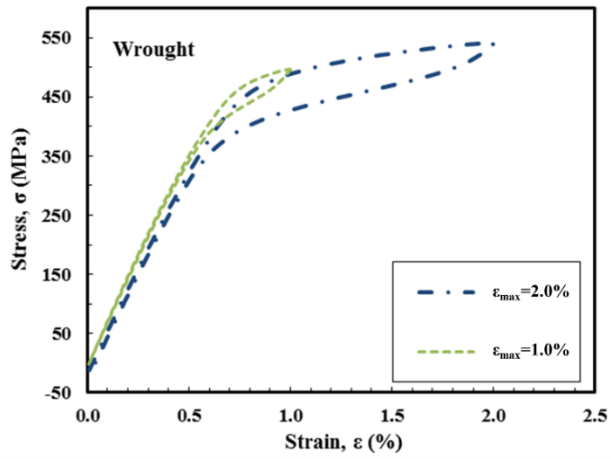

b

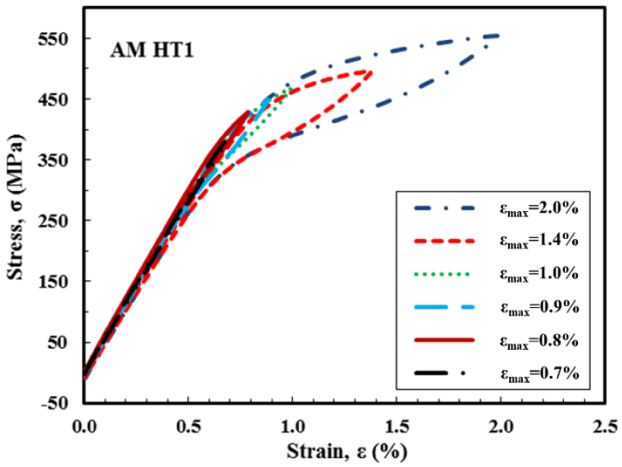

c

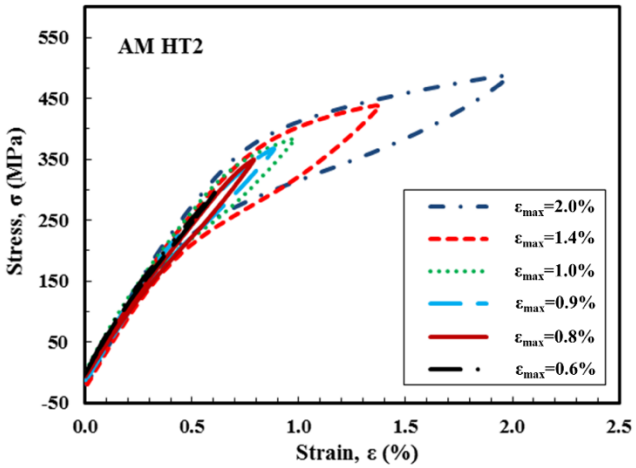

Fig. 6. First cycle stress-strain response of NiTi at different maximum strain levels: (a) wrought (Mahtabi et al., 2015b), (b) AM HT1, and (c) AM HT2.

Similar to other metallic materials, cyclic deformation behavior of the superelastic NiTi evolves with increasing number of cycles of loading. However, the stress-strain response reaches a stable state after a limited number of cycles (~150-200 cycles) as also reported in other studies for wrought NiTi (Mahtabi et al., 2015b). Miyazaki et al., (Miyazaki et al., 1986) reported that the evolution of the cyclic stress-strain response for NiTi typically occurs in the form of change in stress-induced martensite start stress, σ_s^{AM}, the size of the hysteresis loop, and sometimes, accumulation of the residual strain. Furthermore, Mahtabi et al. (Mahtabi et al., 2015b) have also reported some cyclic stress hardening and mean stress relaxation for wrought superelastic NiTi and stated that the amount of stress hardening and mean stress relaxation were greater for tests with larger mean strains, where the volume fraction of the martensitic phase was larger.

Cyclic stress-strain responses of the first, tenth and mid-life cycles at ε_{max}=2.0% for three different NiTi alloys, employed in this study (i.e. wrought, AM HT1 and HT2), are presented in Fig. 7. According to Fig. 7, with increasing number of cycles of loading, a decrease in the A→M start stress, σ_s^{AM}, as well as an increase in the stress corresponding to the maximum strain (i.e. 2.0%) can be noticed for NiTi in all three conditions. Moreover, Miyazaki et al., (Miyazaki et al., 1986) showed that the area surrounded by loading and unloading paths, i.e. hysteresis loop, decreases with increasing number of cycles until the stress-strain response reaches a stable state). The increase in the stress range with increasing number of cycles of loading indicates a cyclic hardening behavior for both wrought and AM NiTi. For all the AM and wrought specimens, the amount of residual strain, probably due to the residual martensitic phase, at zero stress was not remarkable, as can be seen in Fig. 7.

a

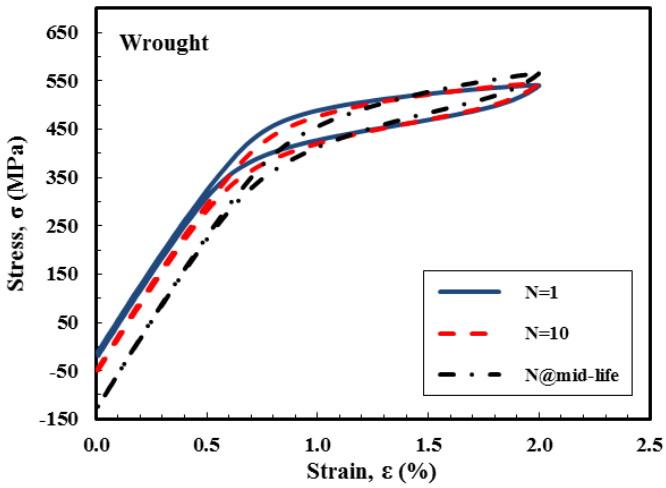

b

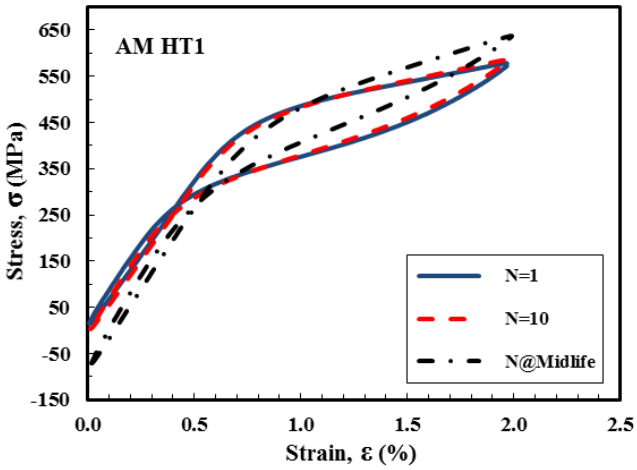

c

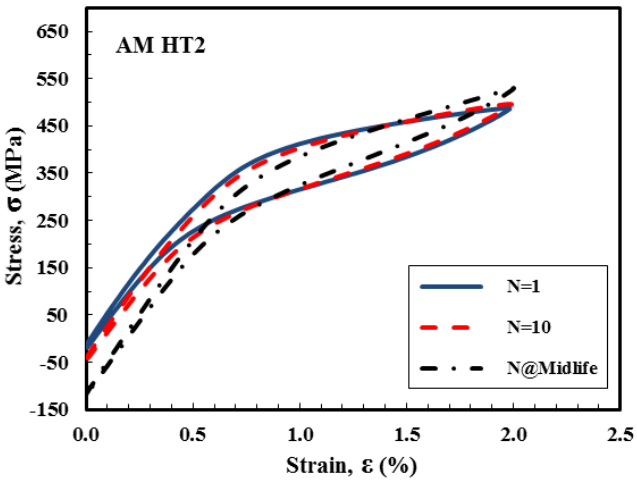

Fig. 7. Cyclic stress-strain response at different cycles of loading for: (a) wrought (Mahtabi et al., 2015b), (b) AM HT1, and (c) AM HT2.

First cycle stress-strain response at ε_{max}=2.0% for all three sets of specimens, including wrought, AM HT1 and AM HT2, are plotted in Fig. 8. As can be seen from this figure, AM HT1 and wrought specimens have very similar stress levels (both A→M start stress, σ_s^{AM}, and maximum stress, σ_{max}) with maximum stress level of AM HT1 being slightly higher than the wrought material. Unlike AM HT1 specimen, the AM HT2 specimen exhibits lower level of σ_s^{AM} and σ_{max} compared to the wrought counterpart. Adjusting the heat treatment to have AM NiTi specimens with two different stress levels provide the opportunity to interpret the experimental fatigue data with respect to stress as well as strain. This is important based on Mahtabi et al.'s (Mahtabi et al., 2015a) argument that the fatigue analysis of superelastic NiTi may yield different results in stress-life and strain-life approaches.

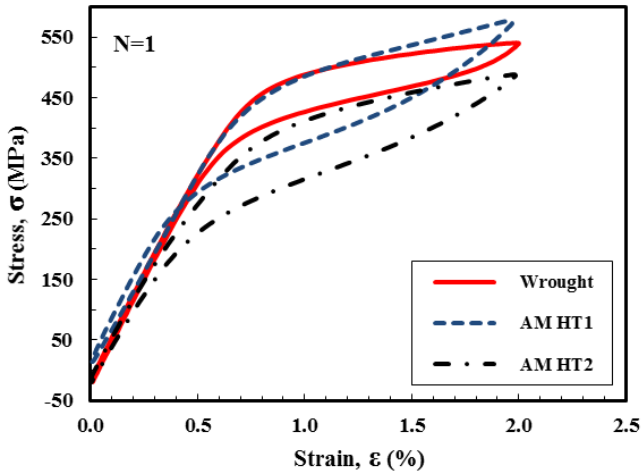

Fig. 8. Comparison of the first cycle stress-strain response of wrought (Mahtabi et al., 2015b) and AM NiTi at ε_{max}=2.0%.

4. Fatigue Behavior and Discussion

4.1 Fatigue Life Behavior

Results from constant amplitude strain-controlled fatigue experiments on wrought and two types of AM NiTi specimens (heat-treated at two different conditions) are presented in this section and discussed in the form of strain-life and stress-life approaches. Experimental measurements of

the fatigue life and corresponding stress response at different strain amplitudes are listed in Table 4 for wrought (Mahtabi et al., 2015b), AM HT1 and AM HT2 NiTi. The values of the stress in this table are obtained from the stable cycle, measured near the mid-fatigue life of the specimen.

Table 4. Summary of the strain-controlled pulsating (R_ε =0) fatigue tests on AM and wrought NiTi.

	ε_{max} (%)	σ_{max} (MPa)	Reversals to Failure, $2N_f$
Wrought (Mahtabi et al., 2015b)	3.0	586	1,271
	3.0	577	1,487
	3.0	575	1,489
	2.0	562	3,542
	2.0	564	4,666
	2.0	570	4,920
	1.0	511	>216,410
AM HT1	2.0	610	634
	2.0	590	1,082
	1.4	553	3,706
	1.4	512	8,508
	1.0	475	24,266
	1.0	496	31,542
	0.9	461	38,922
	0.9	498	48,312
	0.8	450	510,428
	0.8	400	>814,574
	0.7	425	>1,541,420
AM HT2	2.0	533	1,394
	2.0	524	1,650
	1.4	500	8,930
	1.4	470	10,368
	1.0	414	25,382
	1.0	350	31,790
	0.8	310	>1,203,274
	0.6	297	>1,861,346

As can be seen in Table 4, AM specimens lasted longer than the wrought specimens, before they failed in the grip. As a result, the high cycle fatigue (HCF) data for both types of AM

specimens include longer fatigue lives, whereas the wrought material could not be tested to longer lives due to the fretting fatigue problem in their grip sections. Moreover, for larger strain levels (i.e. $\varepsilon_{max} > 1.0\%$), AM HT1 specimens exhibited higher stress response as compared to AM HT2 specimens.

The strain-life (ε_{max}-N) data from strain-controlled fatigue experiments for the three batches of specimens investigated in this study is presented in Fig. 9a. A run-out life of 10^5 cycles was considered in this study. Data points indicated by arrow are specimens that failed in the grip, demonstrating the actual fatigue life to be longer than that reported here. As can be seen from Fig. 9a, fatigue lives of both sets of AM specimens are shorter than those for wrought NiTi in both low cycle (i.e. larger maximum strains) and high cycle (i.e. smaller maximum strains) fatigue regimes. In short life regime, for instance, the average fatigue life at $\varepsilon_{max} = 2.0\%$ for wrought NiTi is a factor of two and six longer than the ones for AM HT2 and HT1 specimens, respectively.

In the HCF regime, however, the main challenge was the grip failure, probably due to the fretting fatigue, that limited the fatigue testing and did not allow continuation of the test to reach failure at the gage section. This challenge was more pronounced for wrought specimens. Despite the fact that the HCF tests on wrought material are not available for very long lives (for example 10^6 cycles), the existing data confirm noticeably reduced fatigue lives of both AM HT1 and HT2 specimens compared to the wrought material (see the data points at $\varepsilon_{max} = 1.0\%$ in Fig. 9a). Comparing the AM NiTi specimens in strain-life plot (i.e. Fig. 9a), the HT2 specimens typically exhibited longer fatigue lives in short life regime, while fatigue lives of HT1 and HT2 specimens were similar in long life regime. These observations may be attributed to the higher stress response of AM HT1 specimens as compared to AM HT2 ones at higher strain levels, i.e. low cycle fatigue (LCF) regime, as seen in Fig. 8 and Table 4. Moreover, it can be seen from Table 4 that for

duplicate tests, the one with larger stress response always yielded shorter fatigue life, which illustrates the significant effect of the maximum stress level on the fatigue behavior of superelastic NiTi.

a

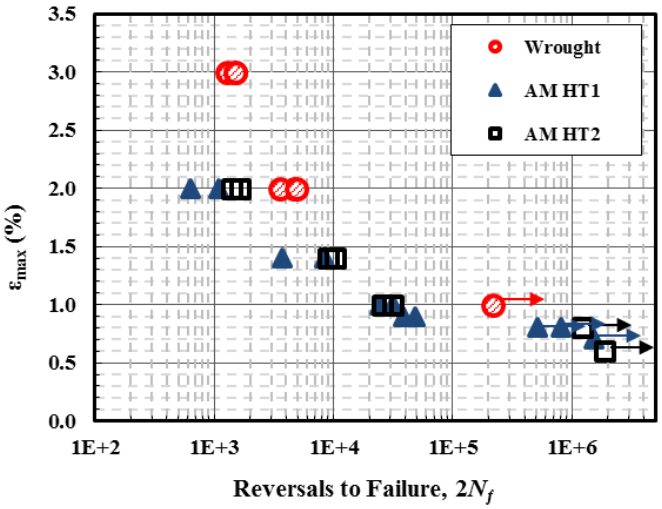

b

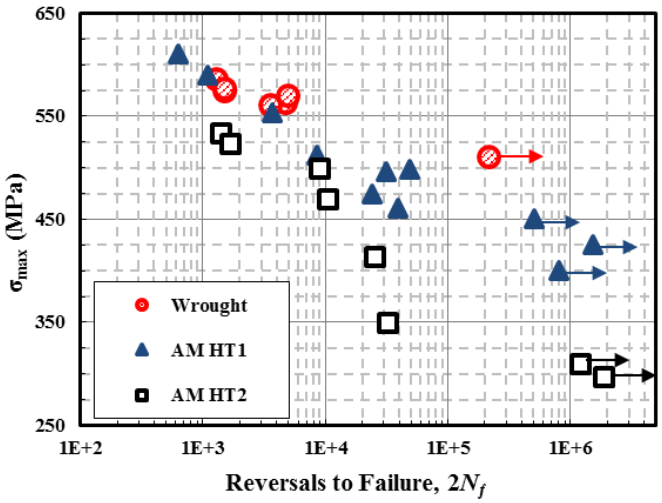

Fig. 9. Comparison of pulsating (R_ε=0) fatigue behavior of AM and wrought (Mahtabi et al., 2015b) NiTi: (a) strain-life data and (b) stress-life data. Data points shown by arrow indicate failure in the grip.

The stress-life fatigue data for wrought, AM HT1 and HT2 specimens are presented and compared in Fig. 9b. As can be seen from this figure, AM specimens, regardless of their heat treatment, yielded shorter fatigue lives as compared to the investigated wrought NiTi, specifically in long life regime. In contrast to the strain-life behavior, the AM HT1 specimens showed longer

fatigue lives than AM HT2 specimens at the same stress level. Moreover, the AM HT1 specimen with ε_{max} = 2.0% that had the shortest fatigue life (i.e. $2N_f$ = 634 reversals) in strain-life plot (in Fig. 9a), appeared to have significantly larger stress level as compared to both wrought and AM HT2 specimens at the same strain level. This may explain the shorter fatigue life observed for this specimen and indicates the coupling effects of strain and stress on fatigue behavior of superelastic NiTi. However, other influential factors, such as microstructural defects, may have also influenced the fatigue resistance of this specimen to some extent. The observed discrepancy in fatigue behavior of superelastic NiTi in stress-life and strain-life approaches was also reported in other studies (Mahtabi et al., 2015a). Therefore, one may conclude that an appropriate fatigue damage model for superelastic NiTi should take into account the synergistic effects of stress and strain components on fatigue resistance, as discussed in detail by Mahtabi and Shamsaei (Mahtabi and Shamsaei, 2016).

As mentioned before, microstructural features of superelastic NiTi can influence the defamation behavior and fatigue resistance of this alloy. Gall and Maier (Gall and Maier, 2002) reported that fatigue resistance of NiTi is affected by the size of Ni_4Ti_3 precipitates. They stated that the fatigue resistance of NiTi is significantly improved by aging, which can produce smaller coherent Ni_4Ti_3 precipitates, compared to the other methods, for almost all orientations. Besides, presence of small coherent Ni_4Ti_3 precipitates in the NiTi leads to a stabilized martensite phase with no dislocation activity due to mechanical cycling, whereas significant dislocation activity can result from mechanical cycling in NiTi specimens with large incoherent Ni_4Ti_3 precipitates.

4.2 Failure Analysis

Fracture surfaces of fatigue specimens fabricated by the employed AM technique were observed using scanning electron microscopy (SEM), and the crack initiation sites were

investigated to determine the cause of fatigue failure in AM NiTi. Failure analysis of the wrought fatigue specimens, corresponding to the data used in this study, was reported elsewhere (Mahtabi et al., 2015b). In wrought material, small inclusion particles such as carbide and oxide particles, as shown in Fig. 10a, were observed to be present at the crack initiation sites. Fractography under SEM illustrated that the location and shape of the inclusion particles are very important factors, influencing the fatigue resistance of wrought superelastic NiTi. Similarly, Eggeler et al., (Eggeler et al., 2004) reported that for wrought NiTi, during cyclic loading, cracks initiated from surface irregularities, scratches, and TiC inclusions, serving as stress concentration points. Furthermore, they mentioned temperature, microstructure, type of loading, the volume and size distributions of inclusion particles as other important factors that can affect the fatigue behavior of NiTi.

Spherical and irregular voids were the two common defect types observed on the fracture surface of AM NiTi specimens in this study, as shown in Figs. 9b and c, respectively. Spherical voids may be resulting from the entrapped gas bubbles, generated when a high laser energy is applied to the melt pool, whereas irregular void, which are mostly un-melted regions, can form due to the lack of fusion and/or low laser penetration depth. For AM parts, presence of various types of microstructural defects with different sizes, shapes, and at different locations (near surface or subsurface) provided various opportunities for the crack initiation, as also stated by Sterling et al. (Sterling et al., 2016). The effects of surface roughness were reduced by machining and polishing the specimens in this study; however, the remaining interior voids and subsurface defects, located near the surface of the specimens, still had significant effects on accelerating the crack initiation. By machining and polishing the specimen's surface, subsurface voids may turn into very small notches on the polished surface, and contribute to the fatigue damage by inducing local stress concentrations.

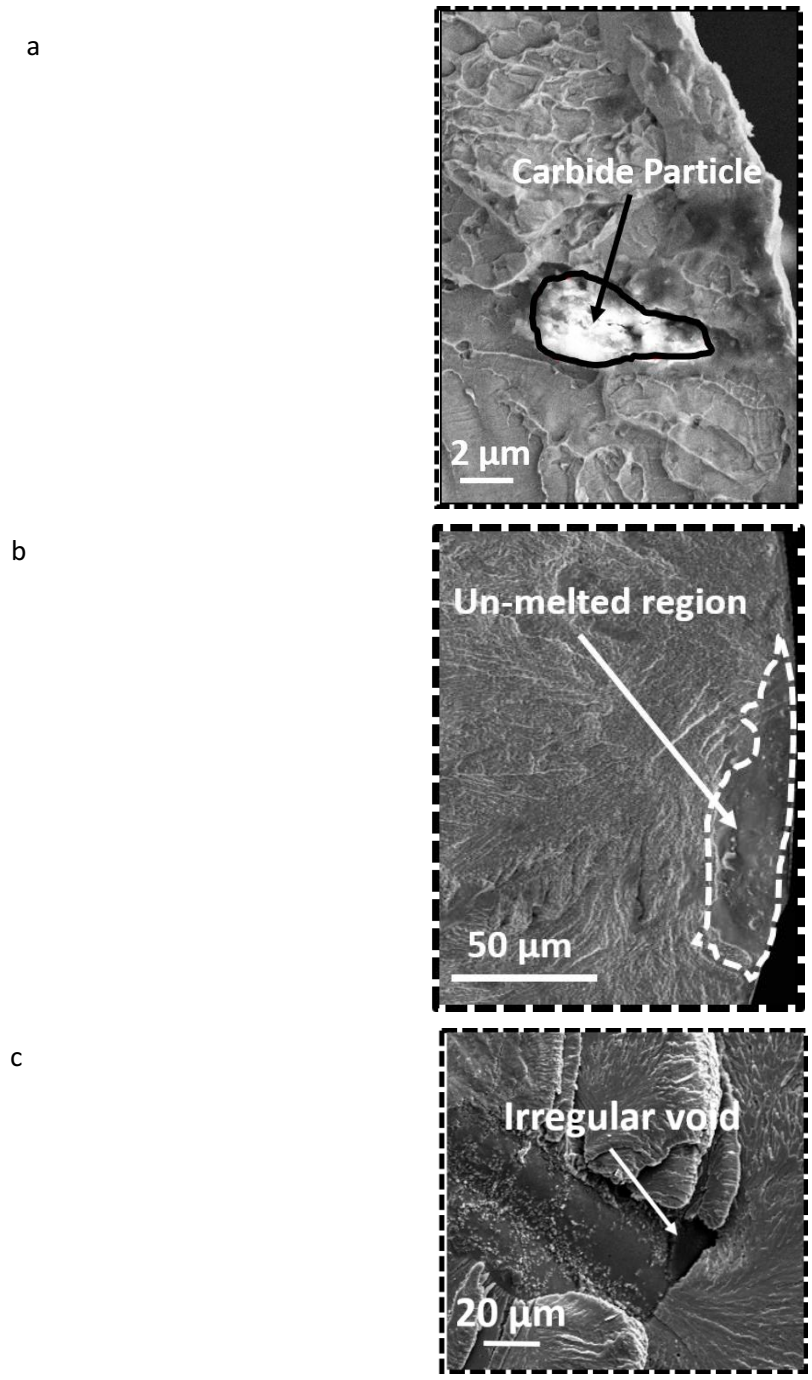

Fig. 10. Magnified fracture surfaces of wrought (a), and two AM fatigue specimens (b and c) showing the presence of different types of defects at crack initiation sites.

For common metals, the presence of defects such as inclusion particles and voids causes stress concentration and increases the localized stress level, to a level typically larger than the yield strength of the material, resulting in localized plastic deformation. This larger stress level

consequently leads to fatigue crack initiation under cyclic loading. For superelastic NiTi, however, the mechanism is different. The localized stress concentration results in a rise in the stress level that forms a localized stress-induced martensitic phase. Following unloading, the localized stress concentration will result in either residual martensitic phase, plastic deformation or a combination of both adjacent to the defect. Presence of plastic deformation and residual martensite may result in crack initiation in superelastic NiTi caused by the sharp interfaces between austenite and martensite phases, as reported by Tabanli et al. (Tabanli et al., 2001).

Fracture surfaces of two AM HT1 specimens, one from the HCF regime (i.e. low strain amplitude) and the other one from the LCF regime (i.e. high strain amplitude) are presented in Fig. 11. Generally, three main regions could be observed on all the fracture surfaces, corresponding to the different stages of the fatigue process: crack initiation, crack growth, and final fracture. Although the crack growth region was not very large for superelastic NiTi and majority of the fatigue life was devoted to the crack initiation stage, the size of the crack growth region was found to depend on the fatigue testing regime (i.e. strain/stress amplitude) (Robertson et al., 2012). A larger crack propagation area could be observed at smaller strain amplitudes (i.e. HCF regime), as shown in Fig. 11a, whereas for higher strain levels (i.e. LCF regime) a smaller crack growth area typically existed, as seen in Fig. 11b.

For the HCF regime, ε_{max} = 0.8%, due to grip failure, fracture at the gage section was only achieved for one AM specimen from HT1 that had a fatigue life of 510,428 reversals. The corresponding fracture surface, presented in Fig. 11a, shows a subsurface defect (an un-melted region) with an approximate size of 55 μm located approximately 550 μm away from the surface. The fracture surface of the specimen tested in LCF regime (ε_{max} = 2.0%, $2N_f$ = 634 reversals), presented in Fig. 11b, reveals a near surface irregular void with an approximate size of 14 μm to

be responsible for crack initiation. This observation, although not statistically significant, may indicate that cracks tend to initiate from subsurface defects in the HCF regime and on-surface/close-to-surface defects in the LCF regime.

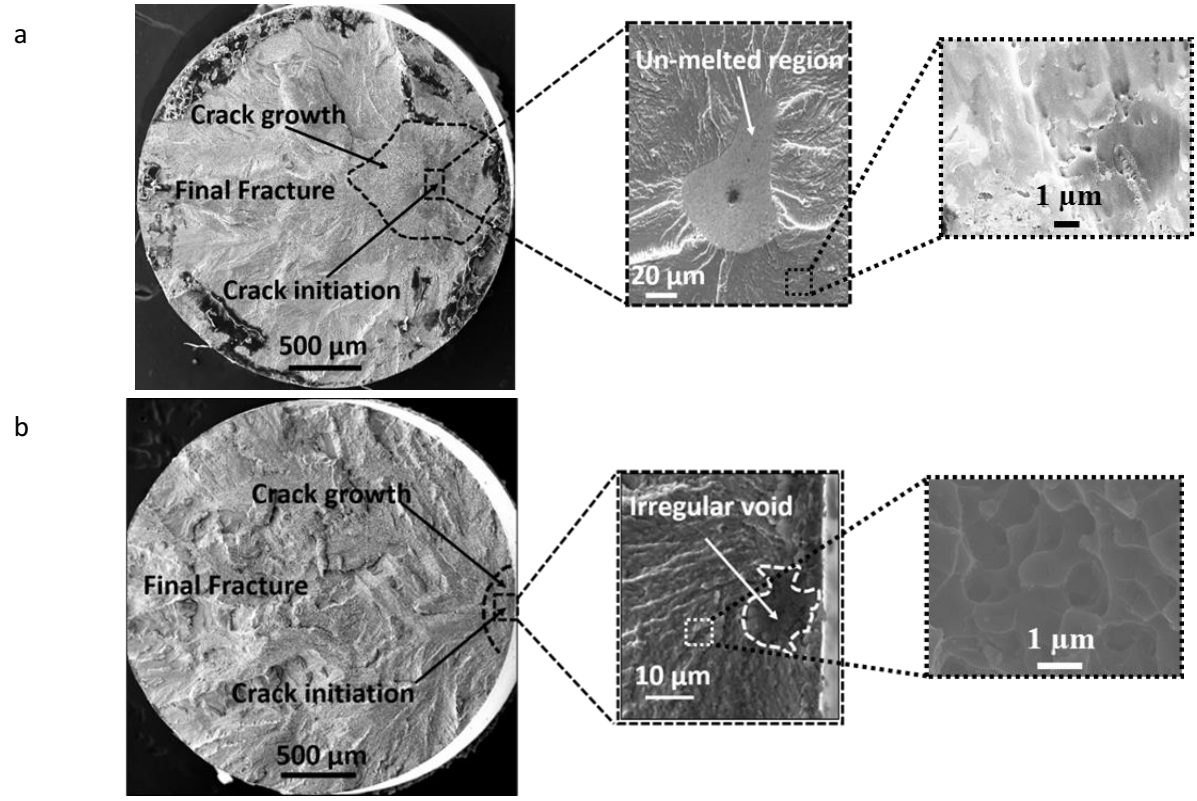

Fig. 11. SEM images of fracture surfaces of two AM HT1 specimens: (a) a HCF specimen at ε_{max}=0.8% and $2N_f$ = 510,428 reversals, and (b) a LCF specimen at ε_{max}=2.0% and $2N_f$ = 634 reversals.

Crack initiation sites, corresponding to two AM HT1 specimens, both tested at 1.4% maximum strain, i.e. mid-cycle fatigue (MCF) regime are presented in Figs. 12a and b. The surface defect in Fig. 12a with an approximate size of 7 µm could have been generated due to the presence of subsurface irregular voids in as-fabricated rod that turned into a surface defect after machining the specimen. Fig. 12b illustrates a specimen with a subsurface void (approximately located 170 µm from the surface) with an approximate size of 140 µm. It should be mentioned that for irregular shape defects, the square root of the defect's area (Murakami, 2002) was considered to

approximate the size of the defect. Fatigue results demonstrate that the specimen with a surface irregular shape defect (Fig. 12a) had almost three times shorter fatigue life than the specimen with subsurface more regular shape defect (Fig. 12b), although the defect size in the latter specimen was significantly larger.

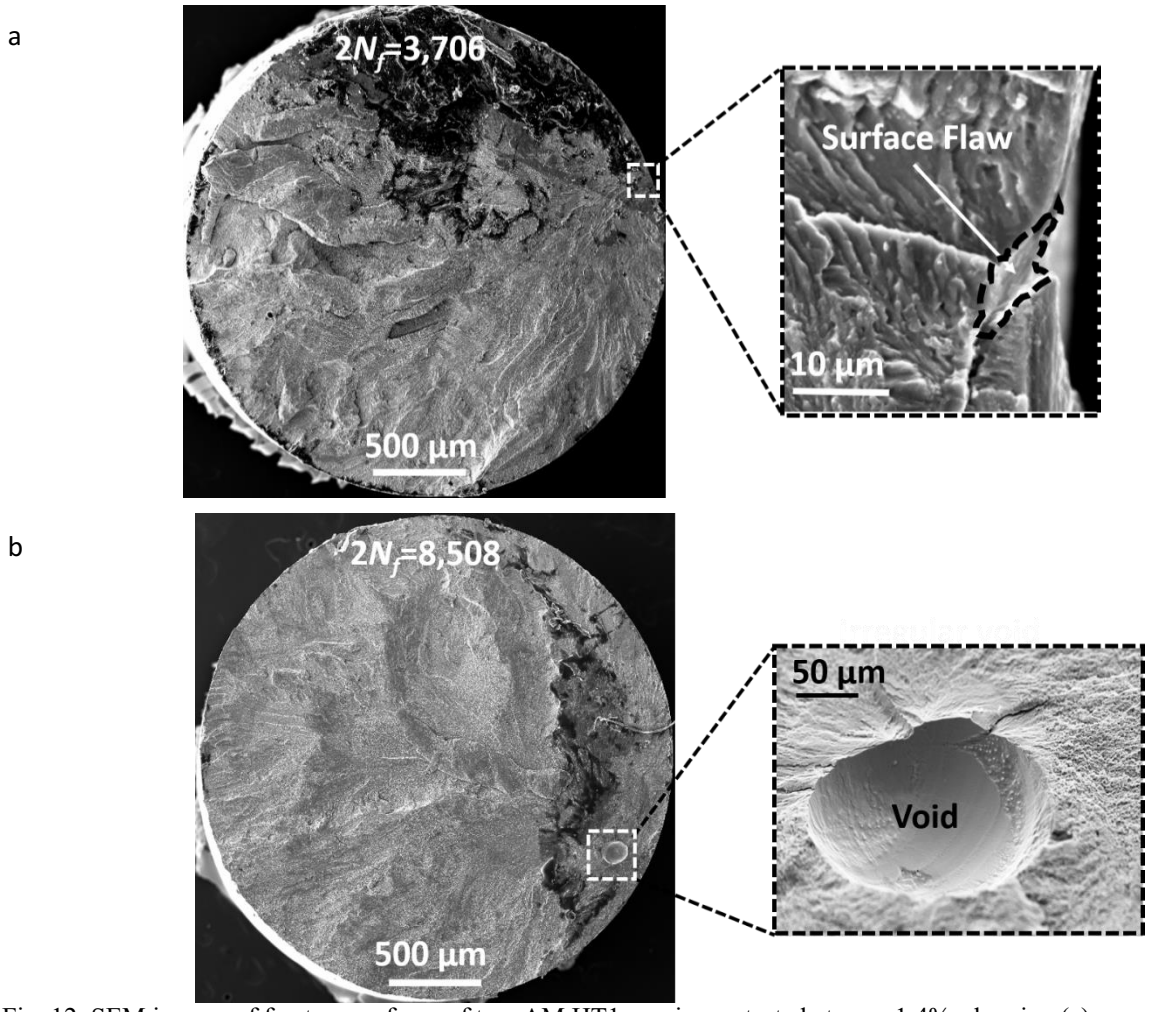

Fig. 12. SEM images of fracture surfaces of two AM HT1 specimens tested at ε_{max}=1.4%, showing (a) a surface defect, and (b) a subsurface void at the crack initiation sites.

Noticeably different fatigue lives observed for the two specimens in Fig. 11 may be attributed to the differences in shape and locations of these defects serving as the crack initiation sites. When a crack forms near surface, it quickly reaches the free surface of the specimen under cyclic

loading. On the free surface, the crack growth is generally accelerated, resulting in a shorter fatigue life. In addition, more irregular shape defects result in higher stress concentrations in their adjacent area, which in turn can accelerate the crack initiation process by increasing the amount of localized plastic deformation and/or residual stress-induced martensitic phase.

Crack initiation sites for two AM HT2 specimens, both tested in LCF regime (2.0% maximum strain) and having slightly different fatigue lives, i.e. $2N_f$ = 1,394 and 1,650 reversals are presented in Figs. 13a and b. As shown in Table 4, both specimens had similar stress levels; the stress level of the specimen with shorter fatigue life being slightly higher. As can be seen in these figures, cracks initiated from un-melted regions near the surface in both specimens. The un-melted regions in Figs. 13a and b have approximate sizes of ~ 65 μm and 190 μm, respectively. The comparable fatigue lives of these two specimens, while having impurities with three times different sizes, may indicate the location of the microstructural defect to be a more influential factor on the fatigue life than the size of the impurity. As mentioned earlier, the specimens broke at the grip in HCF tests of both AM HT1 and HT2, except for one AM HT1 specimen (Fig. 11a); thus, there were not any fracture surfaces for AM HT2 at the HCF regime to be investigated.

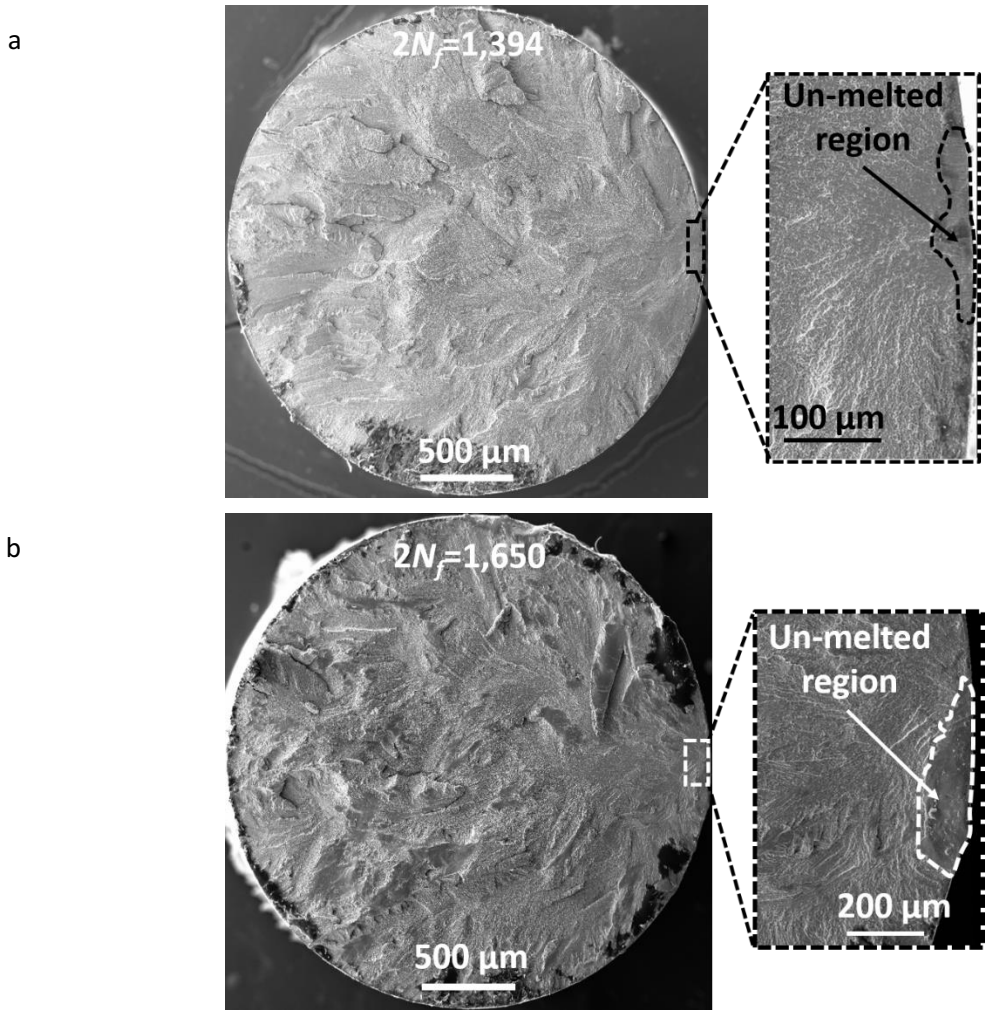

Fig. 13. SEM images of fracture surfaces of two AM HT2 specimens tested in LCF at ε_{max}=2.0%, showing an un-melted region at the crack initiation site.

Fracture surfaces of two AM HT2 specimens tested at 1.4% maximum strain, belonging to the MCF regime, are presented in Fig. 14. It can be seen for both tests that cracks initiated from subsurface voids, approximately located at 180 µm and 105 µm from the surface, in Figs. 14a and b, respectively. The corresponding voids had approximate sizes of 25 µm and 155 µm. It should also be mentioned that the specimen with shorter fatigue life and a larger, more regular shape void had 6% larger stress level, as listed in Table 4. Therefore, slightly different fatigue lives observed for these two specimens, while having noticeably different defects (i.e. size, shape, location) at the crack initiation sites, may indicate the more dominant effects of the stress level and the defect's shape, as compared to the defect's size, on the fatigue behavior.

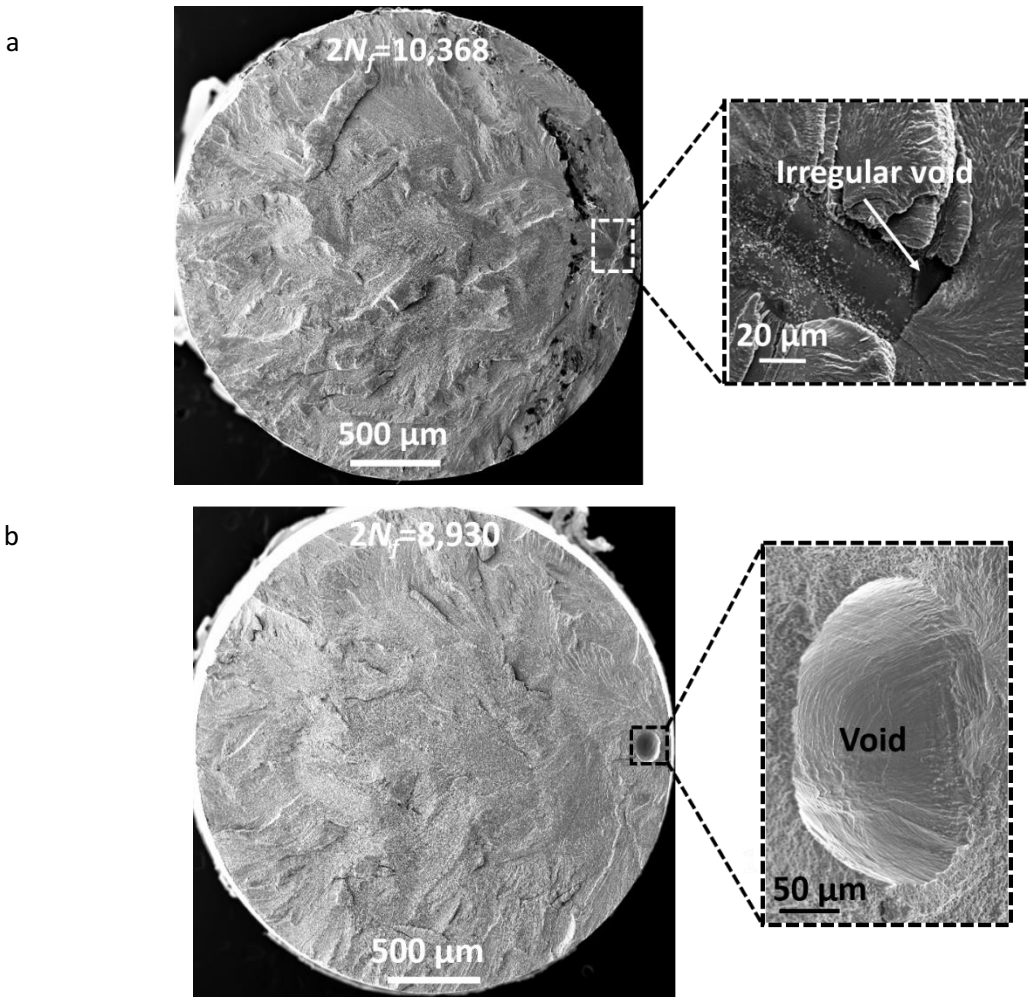

Fig. 14. SEM images of the fracture surfaces of two AM HT2 specimens tested at ε_{max} = 1.4%, showing (a) a smaller irregular shape void, and (b) a larger regular shape void at crack initiation sites at different distances from the surface.

In order to study the effects of heat treatment on the fatigue behavior and damage mechanisms of AM NiTi specimens, the differences in fatigue life and the fracture surfaces of AM HT1 and HT2 specimens can be investigated. A comparison of the fracture surfaces of AM HT1 and AM HT2 specimens in the LCF regime, tested at 2.0% maximum strain, can be made from Fig. 11b and Fig. 13. Cracks in both specimens originated due to the near surface defects (irregular void for AM HT1 and un-melted region for AM HT2). AM HT2 specimens had longer fatigue lives which were more than twice as long than that of AM HT1 specimen. The longer fatigue lives of the AM HT2 specimens, while having larger defects at their crack initiation site, may be attributed to the

lower stress levels of this specimens (average σ_{max} = ~ 530 MPa) as compared to the stress level of AM HT1 specimen (σ_{max} = 610 MPa).

Comparisons of the fatigue lives of AM HT1 and HT2 specimens tested at ε_{max} = 1.4% (i.e. MCF regime) can be made based on Figs. 12 and 14. Figs. 12a and 14a show two relatively small irregular shape voids at the crack initiation sites, the void on AM HT1 is located on the surface of the specimen, while the void on AM HT2 specimen is 180 μm away from the surface. The maximum stress values for AM HT1 specimen (Fig. 12a) and AM HT2 specimen (Fig. 14a) were 553 MPa and 470 MPa, respectively. Since the AM HT1, in this case, had three times shorter fatigue life, while the void in AM HT2 was almost three times larger, one may conclude that the stress level and the defect's location have larger effects on the fatigue resistance of AM NiTi than the defect's size.

Similar microstructural defects (i.e., voids) on both fracture surfaces in Figs. 12b and 14b are noticeable. Moreover, the stress levels of the two specimens were about the same (512 MPa for HT1 and 500 MPa for HT2). Therefore, the comparable fatigue lives (i.e. $2N_f$ = 8,508 and 8,930 reversals) obtained for these specimens can be explained by their similar fatigue related microscopic (such as defect's type, shape and location) as well as macroscopic (such as stress and strain levels) features. These observations as well as other analogies and differences reported before in Figs. 11 to 14, indicate that a reliable fatigue life prediction may be obtained by developing (or calibrating) a microstructure-sensitive model for fatigue analysis of AM NiTi, similar to the one utilized by Torries et al. (Torries et al., 2016). The microstructure-sensitive fatigue model should be able to account for the effects of microstructural features such as type, size, shape, and location of defects on the fatigue behavior. However, calibrating such models are cumbersome and requires extensive experimental and analytical efforts. On the other hand, based

on Table 4, it is clear that regardless of the size, shape, and location of the microstructural defect, the fatigue life was found to always be shorter for the duplicate specimen with higher stress response. This observation indicates that the stress may be the most influential factor on the fatigue behavior of superelastic NiTi, as also stated before by Mahtabi and Shamsaei (Mahtabi and Shamsaei, 2015a).

Considering the fact that a major portion of fatigue life of superelastic NiTi is spent in the fatigue crack initiation stage, which mainly forms around the microstructural defects such as voids, it is crucial to minimize such defects to fabricate more fatigue resistant AM NiTi parts. Process parameters optimization in this study, similar to other investigations conducted on AM parts (Yadollahi et al., 2016), was carried out to maximize the density, measured using Archimedes' principle, to get as close as possible to the density of wrought NiTi. Presence of the voids on the fracture surface of the fatigue specimens, as shown in Figs. 10 through 14, while having a very high density (99.8% of the wrought NiTi) can be due to two possibilities. Either there was a small number of voids in the as-fabricated AM NiTi rods, or the voids had very small volumes, and were most likely planar, similar to the ones shown in Fig. 13.

On the other hand, since the NiTi specimens fracture soon after the crack initiation occurs, even the presence of a few three-dimensional voids, serving as the crack initiation sites, may be enough to accelerate the fatigue failure in AM NiTi specimens. Thus, presence of many planar-small volume voids or a few three-dimensional voids, while not greatly influencing the density of the part, can significantly reduce the fatigue resistance. Consequently, optimizing the process parameters for AM NiTi parts, based on density, as the only optimization objective, may not be adequate to improve their fatigue behavior, as also discussed by Yadollahi et al. (Yadollahi et al., 2016). Further investigations are then needed to determine the appropriate AM process parameters

for manufacturing NiTi parts, considering the effects of type, shape and size of possible microstructural defects on the fatigue behavior, together with maximizing the density.

5. Conclusions

In this study, strain-controlled cyclic deformation and fatigue behavior of AM superelastic NiTi alloys were analyzed experimentally under pulsating (R_ε=0) cyclic loads and the results were compared to wrought superelastic NiTi. The following conclusions can be drawn based on experimental observations and analyses performed:

1. Mechanical properties of AM NiTi, such as modulus of elasticity and loading/unloading stress plateaus, can be adjusted by appropriate heat treatment processes, i.e. combination of annealing and cooling steps. This enables fabrication of NiTi parts with tailored mechanical properties for specific applications such as for bio-implants.
2. Due to the presence of microstructural defects in AM NiTi specimens, they exhibited lower elongation to failure as compared to the wrought material.
3. Fatigue analysis of AM NiTi specimens may yield different results depending on the approach employed, i.e. stress-life or strain-life. Among AM specimens, AM HT2, with lower plateau stress, showed slightly longer fatigue lives in strain-life approach, while exhibited shorter fatigue lives in stress-life approach. Therefore, one can conclude that both stress and strain terms are influential factors on the fatigue behavior of superelastic NiTi. As a result, depending on the application, i.e. load- or deformation-bearing, the fatigue analysis should be conducted utilizing either stress-life or strain-life approach.
4. Although machining and polishing can reduce the surface roughness and associated notch effects on the fatigue behavior of AM NiTi specimens, some subsurface voids can come to

the surface and form new surface flaws. These surface flaws can serve as desired locations for fatigue cracks to initiate.

5. AM NiTi specimens exhibited shorter fatigue lives, specifically in high cycle fatigue regime, as compared to the wrought material mainly due to the existence of microstructural defects.
6. Location, shape (irregular or spherical shape), and size of the defects were the major factors affecting the fatigue resistance of superelastic AM NiTi. Stress response was found to be another major factor with higher stress response often resulting in a shorter fatigue life.
7. Optimizing the AM process parameters solely based on maximizing density, measured using Archimedes' principle, may not be appropriate to enhance the fatigue resistance of AM fabricated NiTi parts. This is due to the fact that most of the defects serving as the crack initiation site are planar voids (e.g., un-melted regions), which do not significantly affect the measured density. As a result, an AM NiTi part with a density close to wrought NiTi may still contain microstructural defects that can be detrimental to its fatigue resistance.

Acknowledgements

Nima Shamsaei's contributions were partially supported by the National Science Foundation under Grant No. 1660446. Experiments were performed at the Center for Advanced Vehicular Systems (CAVS) at Mississippi State University.

References

ASTM B214−15, 2011. Standard test method for sieve analysis of metal powders. ASTM International, West Conshohocken, PA.

ASTM E606 / E606M-12, 2012. Test method for strain-controlled fatigue testing (No. E606-NaN-12), E08. ASTM International, West Conshohocken, PA.

Azimi, M., Rasoulnia, A., Lin, Z. and Pan, H., 2017. Improved semi- active control algorithm for hydraulic damper- based braced buildings. Structural Control and Health Monitoring. DOI: 10.1002/stc.1991.

Bagheri, A., Shamsaei, N. and Thompson, S.M., 2015, November. Microstructure and Mechanical Properties of Ti-6Al-4V Parts Fabricated by Laser Engineered Net Shaping. In ASME 2015 International Mechanical Engineering Congress and Exposition (pp. V02AT02A005-V02AT02A005). American Society of Mechanical Engineers.

Bernard, S., Balla, V.K., Bose, S. and Bandyopadhyay, A., 2012. Compression fatigue behavior of laser processed porous NiTi alloy. Journal of the mechanical behavior of biomedical materials, 13, pp.62-68.

Bian, L., Thompson, S.M. and Shamsaei, N., 2015. Mechanical properties and microstructural features of direct laser-deposited Ti-6Al-4V. Jom, 67(3), pp.629-638.

Bram, M., Ahmad-Khanlou, A., Heckmann, A., Fuchs, B., Buchkremer, H.P. and Stöver, D., 2002. Powder metallurgical fabrication processes for NiTi shape memory alloy parts. Materials Science and Engineering: A, 337(1), pp.254-263.

Carpenter, B. and Lyons, J., 2001. EO-1 technology validation report: Lightweight flexible solar array experiment. NASA/GSFC. Last updated: August, 8.

Chu, C.L., Chung, C.Y., Lin, P.H. and Wang, S.D., 2004. Fabrication of porous NiTi shape memory alloy for hard tissue implants by combustion synthesis. Materials Science and Engineering: A, 366(1), pp.114-119.

Drexel, M.J., Selvaduray, G. and Pelton, A., 2006, May. The effects of cold work and heat treatment on the properties of nitinol wire. In Masters Abstracts International (Vol. 45, No. 04).

Eggeler, G., Hornbogen, E., Yawny, A., Heckmann, A. and Wagner, M., 2004. Structural and functional fatigue of NiTi shape memory alloys. Materials Science and Engineering: A, 378(1), pp.24-33.

Elahinia, M., Moghaddam, N.S., Andani, M.T., Amerinatanzi, A., Bimber, B.A. and Hamilton, R.F., 2016. Fabrication of NiTi through additive manufacturing: A review. Progress in Materials Science, 83, pp.630-663.

Frazier, W.E., 2014. Metal additive manufacturing: a review. Journal of Materials Engineering and Performance, 23(6), pp.1917-1928.

Gall, K. and Maier, H.J., 2002. Cyclic deformation mechanisms in precipitated NiTi shape memory alloys. Acta Materialia, 50(18), pp.4643-4657.

Gall, K., Sehitoglu, H., Chumlyakov, Y.I., Zuev, Y.L. and Karaman, I., 1998. The role of coherent precipitates in martensitic transformations in single crystal and polycrystalline Ti-50.8 at% Ni. Scripta materialia, 39(6), pp.699-705.

Griffith, M.L., Keicher, D.L., Romero, J.A., Atwood, C.L., Harwell, L.D., Greene, D.L. and Smugeresky, J.E., 1996. Laser engineered net shaping (LENS) for the fabrication of metallic components (No. SAND--96-1293C; CONF-9605172--1). Sandia National Labs., Albuquerque, NM (United States).

Gu, D.D., Meiners, W., Wissenbach, K. and Poprawe, R., 2012. Laser additive manufacturing of metallic components: materials, processes and mechanisms. International materials reviews, 57(3), pp.133-164.

Hartl, D.J. and Lagoudas, D.C., 2007. Aerospace applications of shape memory alloys. Proceedings of the Institution of Mechanical Engineers, Part G: Journal of Aerospace Engineering, 221(4), pp.535-552.

Hey, J.C. and Jardine, A.P., 1994. Shape memory TiNi synthesis from elemental powders. Materials Science and Engineering: A, 188(1-2), pp.291-300.

Karaca, H.E., Saghaian, S.M., Ded, G., Tobe, H., Basaran, B., Maier, H.J., Noebe, R.D. and Chumlyakov, Y.I., 2013. Effects of nanoprecipitation on the shape memory and material properties of an Ni-rich NiTiHf high temperature shape memory alloy. Acta Materialia, 61(19), pp.7422-7431.

Mahtabi, M.J. and Shamsaei, N., 2016. A modified energy-based approach for fatigue life prediction of superelastic NiTi in presence of tensile mean strain and stress. International Journal of Mechanical Sciences, 117, pp.321-333.

Mahtabi, M.J., Shamsaei, N. and Mitchell, M.R., 2015a. Fatigue of Nitinol: The state-of-the-art and ongoing challenges. Journal of the mechanical behavior of biomedical materials, 50, pp.228-254.

Mahtabi, M.J., Shamsaei, N. and Rutherford, B., 2015b. Mean strain effects on the fatigue behavior of superelastic nitinol alloys: An experimental investigation. Procedia Engineering, 133, pp.646-654.

Meier, H., Haberland, C. and Frenzel, J., 2011. Structural and functional properties of NiTi shape memory alloys produced by selective laser melting. Innovative developments in design and manufacturing: advanced research in virtual and rapid prototyping, pp.291-296.

Miyazaki, S., Imai, T., Igo, Y. and Otsuka, K., 1986. Effect of cyclic deformation on the pseudoelasticity characteristics of Ti-Ni alloys. Metallurgical and Materials Transactions A, 17(1), pp.115-120.

Moghaddam, N.S., Elahinia, M., Miller, M. and Dean, D., 2014, September. Enhancement of bone implants by substituting nitinol for Titanium (Ti-6Al-4V): A modeling comparison. In ASME 2014 Conference on Smart Materials, Adaptive Structures and Intelligent Systems (pp. V001T03A031-V001T03A031). American Society of Mechanical Engineers.

Murakami, Y., 2002. Metal fatigue: effects of small defects and nonmetallic inclusions. Elsevier.

Nishida, M., Wayman, C.M. and Honma, T., 1986. Precipitation processes in near-equiatomic TiNi shape memory alloys. Metallurgical and Materials Transactions A, 17(9), pp.1505-1515.

Otsuka, K. and Ren, X., 2005. Physical metallurgy of Ti–Ni-based shape memory alloys. Progress in materials science, 50(5), pp.511-678.

Otsuka, K. and Wayman, C.M. eds., 1999. Shape memory materials. Cambridge university press.

Pelton, A.R., Dicello, J. and Miyazaki, S., 2000. Optimisation of processing and properties of medical grade Nitinol wire. Minimally Invasive Therapy & Allied Technologies, 9(2), pp.107-118.

Plotino, G., Grande, N.M., Cordaro, M., Testarelli, L. and Gambarini, G., 2009. A review of cyclic fatigue testing of nickel-titanium rotary instruments. Journal of endodontics, 35(11), pp.1469-1476.

Rahim, M., Frenzel, J., Frotscher, M., Pfetzing-Micklich, J., Steegmüller, R., Wohlschlögel, M., Mughrabi, H. and Eggeler, G., 2013. Impurity levels and fatigue lives of pseudoelastic NiTi shape memory alloys. Acta Materialia, 61(10), pp.3667-3686.

Robertson, S.W., Pelton, A.R. and Ritchie, R.O., 2012. Mechanical fatigue and fracture of Nitinol. International Materials Reviews, 57(1), pp.1-37.

Saedi, S., Turabi, A.S., Andani, M.T., Haberland, C., Elahinia, M. and Karaca, H., 2016. Thermomechanical characterization of Ni-rich NiTi fabricated by selective laser melting. Smart Materials and Structures, 25(3), p.035005.

Saedi, S., Turabi, A.S., Andani, M.T., Haberland, C., Karaca, H. and Elahinia, M., 2016. The influence of heat treatment on the thermomechanical response of Ni-rich NiTi alloys manufactured by selective laser melting. Journal of Alloys and Compounds, 677, pp.204-210.

Schüller, E., Bram, M., Buchkremer, H.P. and Stöver, D., 2004. Phase transformation temperatures for NiTi alloys prepared by powder metallurgical processes. Materials Science and Engineering: A, 378(1), pp.165-169.

Sehitoglu, H., Anderson, R., Karaman, I., Gall, K. and Chumlyakov, Y., 2001. Cyclic deformation behavior of single crystal NiTi. Materials Science and Engineering: A, 314(1), pp.67-74.

Shamsaei, N., Yadollahi, A., Bian, L. and Thompson, S.M., 2015. An overview of Direct Laser Deposition for additive manufacturing; Part II: Mechanical behavior, process parameter optimization and control. Additive Manufacturing, 8, pp.12-35.

Shao, S., Mahtabi, M.J., Shamsaei, N. and Thompson, S.M., 2017. Solubility of argon in laser additive manufactured α-titanium under hot isostatic pressing condition. Computational Materials Science, 131, pp.209-219.

Shishkovsky, I., Yadroitsev, I. and Smurov, I., 2012. Direct selective laser melting of nitinol powder. Physics Procedia, 39, pp.447-454.

Speirs, M., Van Hooreweder, B., Van Humbeeck, J. and Kruth, J.P., 2017. Fatigue behaviour of NiTi shape memory alloy scaffolds produced by SLM, a unit cell design comparison. Journal of the Mechanical Behavior of Biomedical Materials, 70, pp.53-59.

Sterling, A.J., Torries, B., Shamsaei, N., Thompson, S.M. and Seely, D.W., 2016. Fatigue behavior and failure mechanisms of direct laser deposited Ti–6Al–4V. Materials Science and Engineering: A, 655, pp.100-112.

Tabanli, R.M., Simha, N.K. and Berg, B.T., 2001. Mean strain effects on the fatigue properties of superelastic NiTi. Metallurgical and Materials Transactions A, 32(7), pp.1866-1869.

Tan, G. and Liu, Y., 2004. Comparative study of deformation-induced martensite stabilisation via martensite reorientation and stress-induced martensitic transformation in NiTi. Intermetallics, 12(4), pp.373-381.

Torries, B., Torries, B., Sterling, A.J., Sterling, A.J., Shamsaei, N., Shamsaei, N., Thompson, S.M., Thompson, S.M., Daniewicz, S.R. and Daniewicz, S.R., 2016. Utilization of a microstructure sensitive fatigue model for additively manufactured Ti-6Al-4V. Rapid Prototyping Journal, 22(5), pp.817-825.

Wu, M.H., 2002. Fabrication of nitinol materials and components. In Materials Science Forum (Vol. 394, pp. 285-292). Trans Tech Publications.

Yadollahi, A., Shamsaei, N., Thompson, S.M., Elwany, A. and Bian, L., 2017. Effects of building orientation and heat treatment on fatigue behavior of selective laser melted 17-4 PH stainless steel. International Journal of Fatigue, 94, pp.218-235.

Yadollahi, A., Shamsaei, N., Thompson, S.M. and Seely, D.W., 2015. Effects of process time interval and heat treatment on the mechanical and microstructural properties of direct laser deposited 316L stainless steel. Materials Science and Engineering: A, 644, pp.171-183.

List of Figures

List of Tables